Development and characterization of (MnZn) ferrite-polyacrylonitrile composite nanofiber membranes for tissue engineering

Emergent Materials (2025) 8:6635–6652
https://doi.org/10.1007/s42247-025-01247-w

ORIGINAL ARTICLE

Development and characterization of (MnZn) ferrite-polyacrylonitrile composite nanofiber membranes for tissue engineering

Baran Sarac[1,2] · Elham Sharifikolouei[3] · Matej Micusik[4] · Alessandro Scalia[3] · Ziba Najmi[3] · Andrea Cochis[3] · Lia Rimondini[3] · Gabriele Barrera[5] · Marco Coisson[5] · Selin Gümrükcü[6] · Eray Yüce[1,7] · A. Sezai Sarac[6]

Received: 18 February 2025 / Accepted: 3 September 2025 / Published online: 9 October 2025

Abstract

This study focuses on the synthesis and characterization of advanced polymeric composite electrospun nanofibers (NFs) containing magnetic oxide nanoparticles (NPs). By leveraging the method of electrospinning, the research aims to investigate polymer composites with enhanced interfacial properties, improved double-layer capacitance, and adequate biocompatibility. Electrospun polyacrylonitrile (PAN) NFs embedded with Fe_2O_3 and MnZn-Ferrite NPs were comprehensively characterized using advanced techniques, i.e., Fourier transform infrared spectroscopy, X-ray photoelectron spectroscopy, high-resolution scanning electron microscopy, X-ray diffraction, and alternating gradient field magnetometry. The incorporation of metal oxide NPs led to significant changes in the thermal, spectroscopic, and morphological properties of the NFs. Spectroscopic analysis confirmed increased oxidation, graphitic carbon content, and the formation of new nitrogen functionalities after heat treatment. Furthermore, interactions between nitrile groups and metal ions were observed, indicating the influence of nanoparticles on surface chemistry. Magnetic characterization demonstrated the potential of these composite NFs to generate magnetic fields for biomedical manipulation. Cytocompatibility studies revealed no significant impact on the viability or morphology of human mesenchymal stromal cells, highlighting their biocompatibility. These findings suggest the promising use of PAN-magnetic NFs in applications including targeted drug administration, magnetic resonance imaging, and magnetic hyperthermia for cancer treatment.

1 Introduction

Iron oxide in fibrous membranes can significantly influence human mesenchymal cell (hMSC) attachment and distribution [1, 2]. Iron oxide nanoparticles (IONPs) embedded in fibrous membranes can modify the surface roughness as well as mechanical, thermal and chemical properties of the membranes [3]. Iron oxide is biocompatible and can promote cell viability, where the inclusion of such nanoparticles into polymeric scaffolds can enhance cell adhesion by providing more binding sites for cell attachment. The presence of iron oxide can support cell attachment without causing cytotoxic effects, making it appropriate for biomedical uses [4–8]. The magnetic nature of iron oxide can be used to manipulate cell distribution and orientation using external magnetic fields. This property may be advantageous for applications in tissue engineering where ultimate control over cell placement is needed [9]. Iron oxide nanoparticles have been found to advance the osteogenesis of human mesenchymal stem cells (hMSCs). For regenerative medicine and tissue engineering applications, the attachment and

✉ Baran Sarac
baransarac@gmail.com

1 Erich Schmid Institute of Materials Science, Austrian Academy of Sciences (ÖAW), Jahnstrasse 12, 8700 Leoben, Austria

2 Chair of Casting Research, Montanuniversität Leoben, Franz Josef-Strasse 18, 8700 Leoben, Austria

3 Department of Health Sciences, Center for Translational Research on Autoimmune and Allergic Diseases-CAAD, Università del Piemonte Orientale UPO, 28100 Novara, Italy

4 Polymer Institute, Slovak Academy of Sciences, Dubravska cesta 9, 84541 Bratislava, Slovakia

5 Istituto Nazionale di Ricerca Metrologica (INRiM), Strada delle Cacce 91, Torino 10135, Italy

6 Department of Chemistry, Istanbul Technical University, 34469 Istanbul, Türkiye

7 Department of Materials Science, Chair of Materials Physics, Montanuniversität Leoben, Franz Josef-Strasse 18, 8700 Leoben, Österreich

subsequent differentiation of hMSCs are critical, making this particularly useful for bone tissue engineering [10]. Incorporating iron oxide nanoparticles can affect the nanostructure and porosity of the fibrous membranes. This can enhance nutrient and oxygen diffusion, promoting better cell growth and distribution [11].

Iron oxide embedded in polymeric fibers can promote angiogenesis, the process through which new blood vessels develop from existing ones. IONPs possess magnetic properties that can be used to enhance angiogenesis. The use of an external magnetic field guides and concentrates therapeutic agents, growth factors, or even cells to specific sites, thereby promoting localized angiogenesis [12, 13]. IONPs can be functionalized to carry and release angiogenic growth factors such as VEGF (vascular endothelial growth factor). When incorporated into polymeric fibers, these nanoparticles can enable a sustained release of growth factors, thereby promoting angiogenesis over an extended period. Iron oxide can improve the overall biocompatibility of the scaffold, enhancing cell viability and proliferation. This supportive environment can facilitate endothelial cell function, which is crucial for new blood vessel formation [14].

Polymeric nanofibers (NFs) have received a great deal of attention due to their remarkable attributes, i.e., well-defined molecular alignment, high porosity, large specific surface area, and unique nanoscale properties [15]. The functionality of electrospun fibers with adjustable polymer composite chemistry offers a versatile platform for exploring diverse applications, including filtration media, sound isolation materials, and sensor components [16, 17]. Nanofibers enable the easy integration of a wide range of therapeutic molecules, improving the capacity for drug loading and promoting controlled, long-term release. Additionally, by controlling the arrangement of polymeric fibers at a larger scale, new possibilities emerge for using them as implantable systems for localized drug delivery [18]. Smart polymer nanofibers demonstrate rapid response times due to their unique structural properties. These characteristics make them ideal for utilization in a variety of applications, including serving as a targeted, implantable platform for controlled biomolecule and drug delivery [19–22]. Magnetic metal oxide nanoparticles can be mixed with the polymer matrix to promote electrical conductivity and thermal properties [23].

Several studies report that electrospun NFs—with diameters ranging from 50 to 1,000 nanometers and composed of materials such as collagen, laminin, polycaprolactone-chitosan blends, and polyvinyl alcohol–chondroitin sulfate—enhance cell viability and enable diverse responses including osteogenic, chondrogenic, and neural differentiation [24–28]. Another advantage is that, unlike traditional culture substrates, NFs are capable of advanced cell generation, such as spheroid formation and long-distance communication [29]. On the downside, until now, many studies have not fully reported scaffold properties and cell culture parameters, limiting reproducibility and cross-study comparison. Another disadvantage is the lack of long-term or in-vivo validation tests in many studies. Also, achieving the full biomimicry of the native extracellular matrix, particularly regarding hierarchical structure and dynamic signaling, remains a challenge [30]. Other factors such as scalability, cost and regulatory approvals impose a barrier for translation to clinical trials [26].

Polyacrylonitrile (PAN) is an important biocompatible polymer recognized for its non-toxicity, nonantigenic activity and ease of use in the development of bio-related nanomaterials. Its suitability for creating these materials is further enhanced by its ability to support the structural and temporal control of peptide self-assembly processes [31]. PAN is a polymeric material commonly employed in membrane technology because of its excellent chemical resistance and strong performance in water filtration applications [32]. Electrospun NF networks can be readily fabricated using PAN polymers. These resulting NF membranes feature a remarkably high specific surface area, a highly porous structure, and finely controlled pore sizes, allowing them to be used in the biomedical field [33–35]. PAN readily forms uniform nanofibers via electrospinning, with consistent diameters typically ranging between 200 and 500 nm. It also boasts strong mechanical strength, thermal stability, and weather resistance—making it structurally suitable for biomedical scaffolds and dressings [36]. For example, it has been found that lower cell viability of Saccharomyces cerevisiae and C. albicans on PAN electrospun nanofibers confirms the antifungal properties [37]. In another study, the surface morphology and chemical composition of the nanofibrous PAN membranes were modified, which led to enhanced antibacterial activity, showing potential in the applications of water filtration [38]. On the other hand, pure PAN is inherently hydrophobic and biologically inert, which can hinder cell attachment and fluid interaction. This necessitates extensive surface modifications to render it suitable for biomedical use [36]. PAN nanofibers were also functionalized with an inexpensive biomolecule Bovine serum albumin (BSA) resulting in biomineralized nanofibers [39]. Investigations of blood-surface interaction with polyacrylonitrile-based membranes during hemodialysis are reported [40]. Electrospun magnetic NF mats including PAN are utilized in magnetic hyperthermia therapy, enabling targeted drug delivery and serving as valuable diagnostic and therapeutic tools in cancer treatment. These mats offer innovative solutions for improving the precision and effectiveness of cancer therapies [41].

PAN and Fe(III) metal-organic framework nanocomposites were created via electrospinning, enhancing cellular interactions with the substrate [42]. In medical magnetic particle imaging (MPI), magnetic nanoparticle contrast agents are safer than other materials with high contrast and better sensitivity [43]. Among them, iron oxide nanoparticle tracers are preferred for MPI. Magnetic iron oxide nanoparticles, i.e., ferrites or MnZn ferrites, have been extensively researched for their possible application in biomedical applications owing to strong magnetization while maintaining superparamagnetic behavior, particularly in MRI and hyperthermia for cancer treatment [44, 45]. Uncoated particles face rapid clearance, poor circulation, and heightened toxicity risk. For this reason, one of the strategies is to blend the NPs with PAN through electrospinning. However, since NPs can aggregate inside the PAN matrix, potentially creating inhomogeneities in magnetic properties and impairing fiber uniformity, electrospinning conditions and amount/shape of NPs need to be optimized [46].

To maximize their effectiveness in this context, it is crucial to develop magnetic nanoparticles that offer high heating efficiency, as this enhances their ability to influence the intracellular environment and generate heat effectively. Thus, the design of magnetic nanoparticle composite NFs might have applications in imaging and magnetic field manipulation. MnZn-Ferrite NPs coated by silica were utilized for in-vivo cell tracking which demonstrated low toxicity and effective cellular internalization [47]. In-vivo tumor imaging in mice was conducted using MnZn-Ferrite nanoparticles coated with silica, demonstrating the nanoparticles' safety, biocompatibility, and suitability for cell labeling and tracking [48]. PEG-coated MnZn-Ferrite NPs showed a great potential to be used as a novel Magnetic resonance imaging contrast agent for the detection of 4T1 breast cancer cells [49].

The primary objective of this study is to demonstrate that ferrite-containing PAN NF composites exhibit improved hMSC adhesion and proliferation compared to plain PAN NFs without compromising biocompatibility. This enhancement is attributed to the interaction between the PAN and magnetic NPs, thereby boosting double-layer capacitance, charge collection efficiency, and overall energy storage performance. PAN-magnetic iron oxide porous NF mats, with the aid of their porous structure, hold promise for both diagnostic and therapeutic applications, offering promising opportunities in various biomedical fields. Their compelling biocompatibility, mechanical robustness, and porous architecture further elevate their suitability for magnetic diagnostics. This enhanced suitability stems from the ability of the homogenously dispersed magnetic particles to effectively detect and monitor various medical conditions [50]. Additionally, iron oxide/poly(m-anthranilic acid)/poly(ε-caprolactone) (PCL) composite NF production and advanced characterizations [51], electrospun polyacrylonitrile/2-(acryloyloxy)ethyl Ferrocenecarboxylate (FcP) NFs [52], and the thermomechanical characteristics of magnetic nanoparticles confined within PAN NFs when subjected to a magnetic field [53] have been recently studied.

In this study, electrospun NF containing metal oxide nanoparticles (Fe_2O_3 and MnZn-Ferrite), fabricated to achieve electrical conductivity and magnetic properties, have undergone comprehensive and advanced characterizations mainly via X-ray photoelectron spectroscopy (XPS), X-ray diffraction (XRD), Fourier transform infrared (FTIR) spectroscopy, and high-resolution scanning electron microscopy (SEM), for the comprehensive understanding the mechanism of interaction between metal oxide and nitrile group of polyacrylonitrile matrix reflecting to the influence of nanoparticles on surface chemistry. Magnetic characterization demonstrated the potential of these composite NFs to generate magnetic fields for biomedical manipulation. Cytocompatibility studies confirmed the materials' biocompatibility, as they did not significantly affect human mesenchymal stromal cell viability or morphology. Cell adhesion and proliferation tests evidenced the enhanced cell-biomaterial interaction with the use of composite NFs.

2 Experimental section

2.1 Material

N, N′-dimethylformamide (DMF ≥ 99.8%), polyacrylonitrile (PAN, $M_{w\_average}$ = 150,000), and indium tin oxide coated polyethylene terephthalate (ITO-PET) sourced from Sigma Aldrich were utilized in the experiments. Iron Oxide Nanopowder (γ- Fe_2O_3) and MnZnFerrite nanoparticules were sourced from US Research Nanomaterials, Inc. and were of analytical grade, utilized in their original form without any further purification.

2.2 Formation of PAN/metal oxide nanoparticle composite nanofibers

The electrospinning precursor was formulated by completely dissolving PAN powder in a DMF-based solvent using a cup horn sonicator to create 100 mL of a 10% PAN solution. For the composite NFs, MnZn-Ferrite (5 wt%, 99.99% purity, ~28 nm diameter near-spherical) and γ-Fe_2O_3 (5 wt%, 99.9% purity, ~10 nm diameter near-spherical) NPs were dispersed in this 10 ml of 10% PAN solution in the same cup horn sonicator by overnight stirring (12 h) to avoid sediment formation and to facilitate homogenous dispersion of

the metal oxide NPs. The electrospinning setup consists of a grounded collector, a syringe pump with a flow rate of 5.5 μL h^{-1} to 20 mL h^{-1}, and a high-voltage DC power supply capable of up to 50 kV. The 0.7 mm syringe needle was connected to a positive electrode. The syringe pump precisely controlled the flow rate of the polymer solution, ensuring a steady supply during electrospinning. The polymer solutions were electrospun in a horizontal configuration onto an aluminum collector. To fabricate NFs, the electrospinning was conducted at room temperature with applied voltages between 10 and 15 kV. The capillary tip was consistently maintained at a distance of approximately 15 cm from the collector, while the solution was supplied at a rate of 1 mL h^{-1}. No visual sedimentation was observed in the syringe after each electrospinning trial, proving the even dispersion of the PAN and metal oxide NPs within the solvent. Heat treatment of some of the NFs was conducted inside a dynamic mechanical analyzer, as previously explained in [53]. In short, the specimens were subjected to a controlled temperature increase from 300 K to 800 K at a uniform 5 K min^{-1} heating rate. The tests were performed under an Ar flow of 20 mL min^{-1} and cooled down in a furnace environment after reaching the maximum temperature.

2.3 Electrochemical impedance spectroscopy

The standard three-electrode system was employed, consisting of PAN/metal oxide nanoparticles-NF mats as the working electrode, Ag/AgCl (3 M KCl) as an aqueous reference electrode, and platinum spiral wire as a counter electrode. Electrochemical impedance spectroscopy measurements were implemented over the frequency range of 100 kHz to 0.01 Hz via Gamry Reference 600 (USA). The EIS test was conducted under open-circuit potential (OCP) conditions. Two electrolyte mediums were used in the electrochemical measurements as 7.4 pH PBS buffer and 0.5 M H_2SO_4.

2.4 Structural analysis

XRD measurement was conducted utilizing a Bruker D2Phaser diffractometer equipped with an LYNXEYE-2 detector, operating in Bragg-Brentano (θ−2θ) configuration. The measurements were performed over an angular range spanning from 5° to 100°, employing Co Kα radiation with a wavelength of 0.17902 nm. Data acquisition was carried out with a step size of 0.005°.

2.5 Spectroscopic analysis

XPS measurements were conducted using a Thermo Scientific Nexsa G2 Surface Analysis System (Thermo Fisher Scientific, UK), featuring a micro-focused, monochromatic Al Kα X-ray source (1486.68 eV). The system utilized an X-ray beam with a diameter of 400 mm. The spectra were collected using a constant analyzer energy mode, employing a pass energy of 200 eV for the survey scans. For detailed measurements, smaller regions were analyzed using a 50 eV pass energy. Charge compensation during the analysis was accomplished through the system's dual beam flood gun. The heat-treated samples were evaluated only by XPS to determine the extent of PAN oxidation and carbon graphitization; however, they were not used in later experiments due to significant changes in surface chemistry. Data acquisition and processing were completed through Thermo Scientific Avantage software, version 6.9.0. Spectral calibration was performed using the automated calibration routine and internal standards of Au, Ag, and Cu provided by the K-Alpha system. The atomic percent surface compositions were assessed by analyzing the integrated peak areas of the identified elements and applying the corresponding sensitivity factors. The concentration fraction of element A was determined by:

$$\%\,A = \frac{I_A/s_A}{\sum\,(I_n/s_n)} \times 100\% \tag{1}$$

where I_n and s_n represent the total integrated peak areas and the Scofield sensitivity factors, both adjusted for the transmission efficiency of the analyzer, respectively. Attenuated total reflectance Fourier-transform infrared (ATR-FTIR) spectroscopy was carried out using a Bruker Vertex 70 ATR spectrometer, operating at a spectral resolution of 0.4 cm^{-1} and spanning a wavenumber range of 600 to 4000 cm^{-1}.

2.6 Morphological analysis

The morphological characteristics of the NFs that were produced were scrutinized by scanning electron microscopy. The investigation by energy dispersive X-ray (EDX) was conducted using a Quanta FEG 250 microscope equipped with an integrated EDX detector. SEM micrographs were captured at Magnification levels of 20k×, 50k×, and 100k×. To ensure sufficient collection of Fe signals, an acquisition time of 20 min was set for the EDX mapping process.

2.7 Magnetic analysis

The room-temperature magnetic properties were tested by a high-sensitivity alternating gradient field magnetometer (AGFM) (Princeton Measurements Corporation, Princeton, NJ, USA). Hysteresis loops were recorded within a ± 10 kOe magnetic field range. The diamagnetic contribution of the sample holder was carefully accounted for and subtracted from the measured data.

2.8 Cytocompatibility analysis

Human bone marrow-derived mesenchymal stromal cells (hBMSCs) were acquired from the American Type Culture Collection (ATCC PCS-500-012) and cultured in low-glucose DMEM (Sigma-Aldrich), enriched with 15% fetal bovine serum (FBS) and 1% penicillin-streptomycin (PS, Sigma-Aldrich), in a 75 cm^2 treated cell culture flask at 37 °C under 5% CO_2. When they attained 80–90% confluence, they were isolated with a trypsin-EDTA solution, harvested, and used for the experiment. Nanofiber membranes were sterilized under UV-C Light for 30min per side and then placed in a sterile 24-well plate. A specific number of cells (1.5×10^4 per specimen) was evenly distributed onto the material surfaces (1 cm × 0.5 cm nanofiber mats) via dropwise seeding and incubated for a few hours in 100 µL of culture medium to ensure proper adhesion and spreading for 2 h (at 37 °C, 5% CO_2). Subsequently, the samples were submerged in a complete fresh culture medium of 1 mL and returned to the incubator for 24 and 48 h. At all relevant intervals, the cellular metabolic activity was assessed using the Alamar Blue assay, following the manufacturer's instructions. Metabolically active cells reduce the blue, nonfluorescent molecule resazurin into the red/violet fluorescent molecule resorufin in direct proportion to cell number. A 0.015% Alamar solution in a complete medium was applied to the seeded scaffolds and incubated for 3 h in the dark. After incubation, 100 µl of the solution was moved to a black plate, and fluorescence was recorded by the Spark spectrophotometer (Tecan, Männedorf, Switzerland) through excitation and emission wavelengths of 530 nm and 590 nm, respectively. During the last time point, the viability of cells is further confirmed using the lactate dehydrogenase (LDH) assay (CyQUANT LDH Cytotoxicity Assay, fluorescence). LDH release was used as a marker of cytotoxicity. LDH activity in the culture medium was quantified via a coupled enzymatic reaction in which LDH catalyzes the conversion of lactate to pyruvate with concomitant NAD^+ reduction, followed by diaphorase-mediated resazurin reduction to fluorescent resorufin (Ex/Em: 560/590 nm). The signal is proportional to LDH levels. The test was conducted according to the manufacturer's instructions, and results are expressed as absolute LDH activity. Viable cells are finally visualized on the materials using the exclusive LIVE/DEAD® assay. This two-color fluorescence-based assay employs Calcein AM (green) and ethidium homodimer-1 (EthD-1, red). Live cells, characterized by high intracellular esterase activity, enzymatically convert the cell-permeant, nonfluorescent Calcein AM into highly fluorescent, green-emitting calcein (Ex/Em 495 nm/515 nm). Conversely, EthD-1 penetrates cells with compromised membranes and emits bright red fluorescence (Ex/Em 495 nm/635 nm). The intact plasma membranes of live cells exclude EthD-1, preventing red fluorescence. The EVOS FLoid Imaging System was employed to capture the images (Thermo Fisher, Massachusetts, USA).

2.9 Cell morphology, adhesion, and proliferation assessment

The morphology and distribution of cells in contact with the materials were evaluated using SEM. After the last time point, cells cultivated on top of the materials were fixed overnight (4 °C) using a solution of glutaraldehyde (2.5% in PBS) to preserve their ultrastructure. Later, specimens were dehydrated using an increasing ethanol scale (70, 90, 100%-I, 100%-II for 1 h each) to remove water from the cells progressively. Finally, specimens were immersed in hexamethyldisilazane (HMDS), a low-tension reagent that quickly dries the specimens, reducing the structural artifacts. Specimens were then coated with a thin layer of gold (10 nm) using a Smart Coater (Jeol, Akishima, Japan) and observed using the JSM-IT500 InTouchScope™ SEM (Jeol).

Cell adhesion and proliferation of cells in contact with the materials were further investigated using RT-PCR and the Click-iT™ EdU proliferation assay (Invitrogen, Thermo Fisher), respectively. For gene expression analysis, total RNA was extracted, and the expression levels of Cadherin-1 (CDH1) and Ki67 were quantified to assess the scaffolds' ability to support hBMSC adhesion and proliferation, respectively. Together with Ki67, the hMSC proliferation was evaluated using the Click-iT™ EdU Proliferation Assay, which utilizes 5-ethynyl-2'-deoxyuridine (EdU), a nucleoside analog incorporated into newly synthesized DNA. Briefly, 24 h after cell seeding onto the Material surfaces, a 2 µM EdU solution was added and incubated overnight. EdU detection was achieved via a copper-catalyzed click reaction between the alkyne group of EdU and azide-modified horseradish peroxidase (HRP), followed by the addition of the Amplex™ UltraRed reagent. The resulting fluorescent signal was measured using the spark spectrophotometer (Ex/Em: 568/585 nm). Lastly, the maintenance of the stemness of cells cultivated on the materials was assessed by evaluating the expression of the stemness markers CD90 and CD105 via RT-PCR. Results and primer sequences are presented in Fig. S1 and Supplementary Table. For all the RT-PCR analyses, the glyceraldehyde 3-phosphate dehydrogenase (GAPDH) was used as the housekeeping gene.

3 Results & discussions

3.1 Possible interaction mechanism

A long-term dispersion ensures that the iron oxide nanoparticles are evenly distributed within the PAN matrix. During this step, the chemical interactions (hydrogen bonding, electrostatic interactions, and coordination bonding) start to play a role in stabilizing the dispersion (Fig. 1). The bonding electrons in the C–N bond are more attracted towards the N atom because of the higher electronegativity of the N atom. Hence, the bonding electrons concentrate more on the N atom, with a partial negative charge on the nitrogen in comparison to the partial positive charge on the carbon atom. The cyanide ion interacts with transition metals to create M–CN bonds (where M refers to Fe or MnZn). The strong attraction of metals to this anion can be explained by its partial negative charge, its small size, and its capacity to participate in π-bonding. This bonding occurs as the metal ion's d orbitals overlap with the π orbitals of the polar C≡N bond.

3.2 Morphology and microstructure

High-resolution SEM images, particularly at high Magnification, demonstrate the formation of uniform NFs along with the distribution of single nanoparticles. The PAN NFs exhibit a narrow size distribution, with diameters averaging 970 ± 110 nm (Fig. 2a). A homogeneous dispersion of NFs is observed over extensive areas of interest (Fig. 2d). Fiber diameter size diminished when particles were included (520 ± 50 nm and 520 ± 90 nm for PAN/γ-Fe_2O_3 and PAN/MnZn-Ferrite, respectively). Partial clustering was observed for both γ-Fe_2O_3 (Fig. 2b, e) and MnZn-Ferrite (Fig. 2c, f) nanoparticles within PAN NFs, which is mainly because ceramic nanoparticles typically have high surface energies, leading to strong interparticle interactions that favor agglomeration overdispersion.

3.3 Molecular structure

FTIR spectroscopy in transmittance mode involves passing an infrared light beam through a sample and measuring the intensity of the transmitted light across different wavelengths. Figure 3 compares the three investigated samples; the main peaks from the PAN samples were marked. A noticeable peak appearance was marked at 2243 and 1450 cm^{-1}, which are attributed to the highly polar nitrile group –C≡N of PAN by the inclusion of nanopowders and is more distinctive for the MnZn-Ferrite due to more interaction [54–57]. The rest of the peaks at 2926 and 1664 cm^{-1} are associated with the $–CH_2–$ and C=O groups in the amide structure by undergoing the partial transformation of nitrile groups to amide groups (–$CONH_2$), respectively [54]. As the peak appearing at 2360 cm^{-1} was also detected in our previous work [53], a possible electrostatic interaction between the partial positive charge of metal oxide nanoparticles and the negative charge on the nitrogen of the cyano groups (C=N) of the PAN, as described in [58]. However, the peaks at ~650 cm^{-1} and 2360 cm^{-1} present only in the NP-containing samples were also attributed to the atmospheric CO_2 [59, 60] since the iron oxide present within the composites is a potential adsorbent for CO_2 [61].

3.4 Crystalline structure

Figure 4 shows the structural state of the PAN, PAN/γ-Fe_2O_3 and PAN/MnZn-Ferrite NF composites. The broad signals at 14.2° and 26.0° confirm the amorphous PAN structure [62]. The peaks at ~35.5°, ~41.6°, and ~50.8° correspond to (220), (311) and (400) planes of the γ-Fe_2O_3 and MnZn-Ferrite peaks, respectively [63, 64]. In comparison to the largest broad peak position of the PAN, a minor displacement of 0.3° in the peak positions of the NP-containing samples towards higher angles can be attributed to the immediate polymer cooling electrospun on the aluminum foil, resulting in polymer contraction and, hence, a decrease in lattice spacing.

3.5 Surface composition and chemical state

XPS confirmed the structure of PAN. Figure 5a displays the survey spectrum with strong signals of C1s, N1s and O1s. We also observed some contamination by sulfur, silicon, and phosphorus from the processing of NFs. These elements were not included in Table S2 since we show results from high-resolution spectra, and we have not performed high resolution from these regions corresponding to the mentioned elements. C1s signals at ca. 285.6 eV corresponding to ─CH_2─ group in PAN (labeled as C1 in Fig. 5b), at ca. 286.4 eV corresponding to ─CH─ in PAN (labeled as C2 in Fig. 5b) and ─C≡N at ca. 287.0 eV confirming the structure of PAN [65]. There is also some adventitious carbon at ca. 284.9 eV and a small portion of sp^2 at ca. 284.2 eV. PAN NFs before heat treatment exhibits only small oxidation, which represents only 2.6 at% of oxygen and only 2.6 at% of pyrrolic nitrogen (Fig. 5c, Table S2). PAN NFs with NPs before heat treatment showed only slightly higher oxidation, ca. 3-3.2 at%, and the NPs are fully covered by PAN. We detected only noisy spectra with the only indication of the presence of Fe_2O_3 (Figure S2 a) in the case of the PAN-Fe_2O_3 sample. In the case of PAN/MnZn-Ferrite there was not even this indication (Figure S2 c, e,f). XPS results of NFs after heat treatment (labeled as "(HT)") indicate an increase in PAN oxidation, and an increase in graphitic

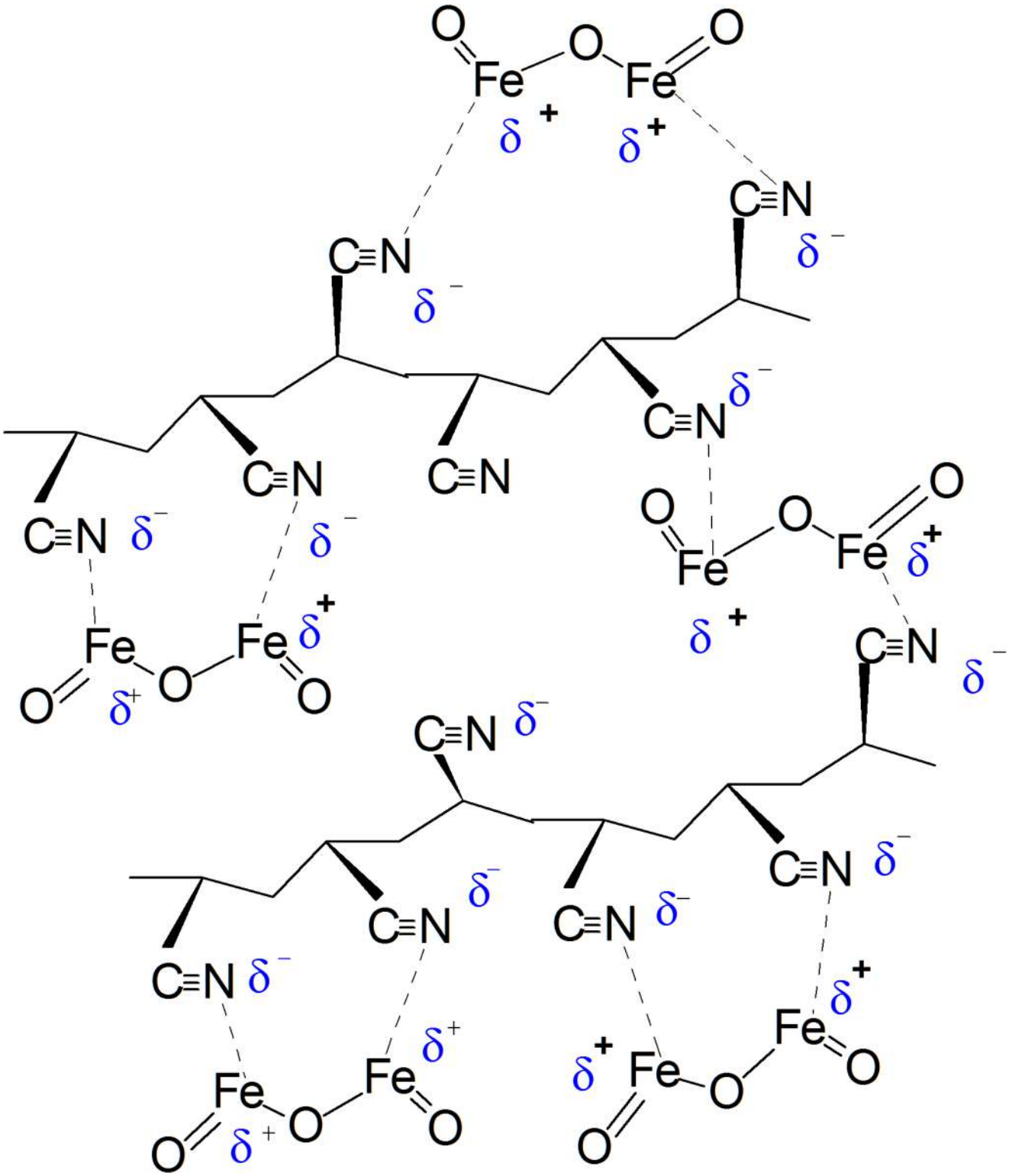

Fig. 1 Scheme of possible interaction of Fe_2O_3 with Polyacrylonitrile

carbon (from ca. 7 at% to ca. 16 at%) is observed (Fig. 5b, Table S2) that is linked to the interaction of hydrogen bonds. After heat treatment, we detected signals coming from NPs, which can be the result of changes in PAN structure (Table S2, Figure S2 b, d, g, h). This is also accompanied by the changes in nitrogen chemistry, and the N1s signal at ca.

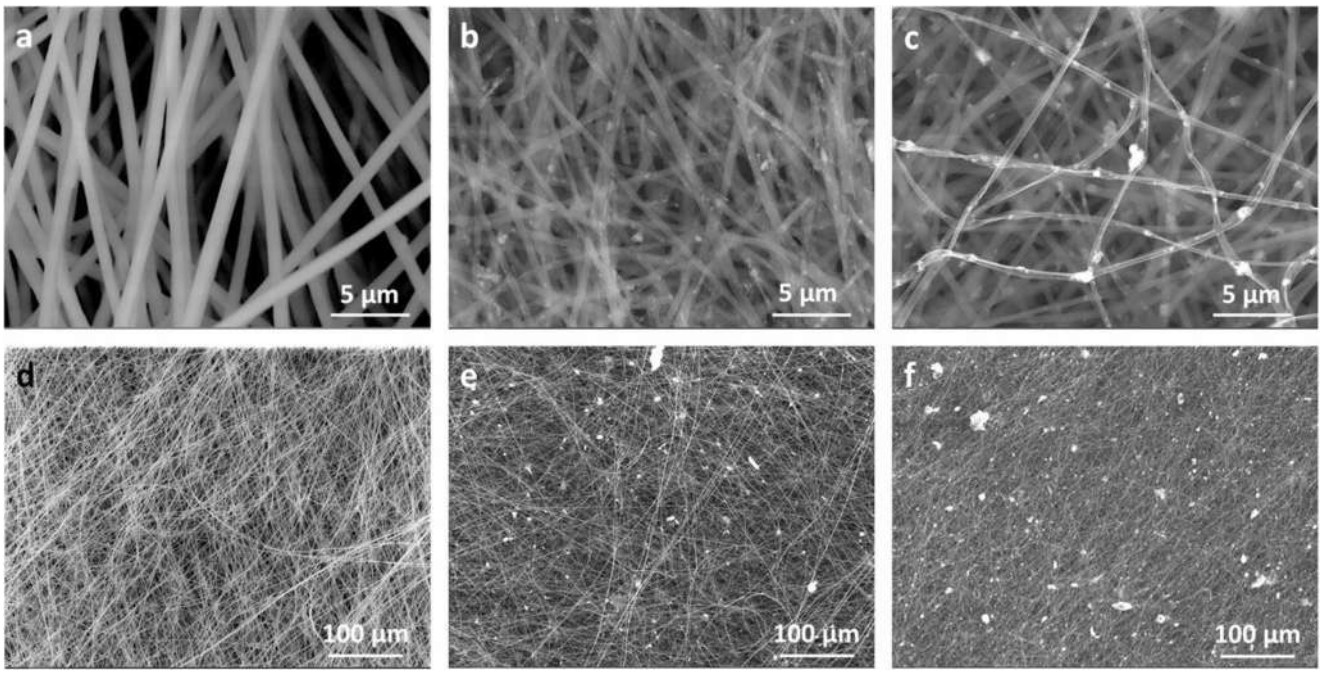

Fig. 2 Enlarged PAN NFs at 20 k× (**a**) without nanoparticles, (**b**) with γ-Fe_2O_3, (**c**) with MnZn-Ferrite. PAN NFs at 1000× (**d**) without nanoparticles, (**e**) with γ-Fe_2O_3, (**f**) with MnZn-Ferrite

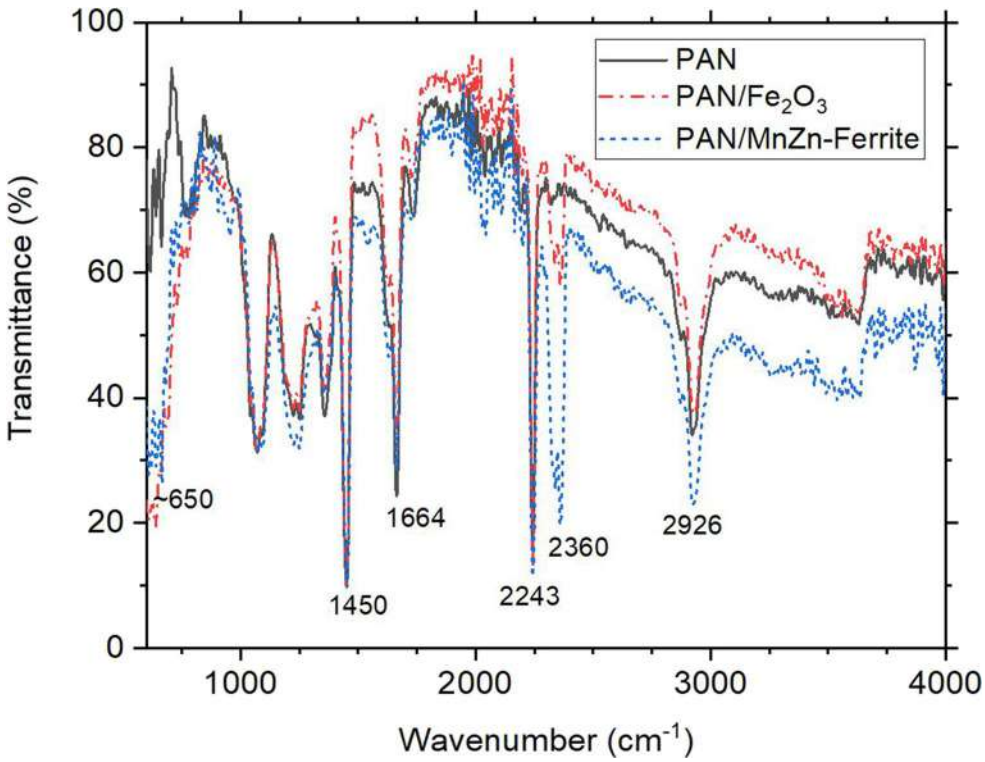

Fig. 3 Spectroscopic analysis of PAN (solid black), PAN/Fe_2O_3 (dash-dot red) and PAN/MnZn-Ferrite (dot blue)

398.8 eV indicates the presence of imine or pyridinic structures. N1s at ca. 400.6 eV indicate the presence of imide or pyrrolic nitrogen during heat treatment, leading to cyclization-induced C=N bond formation [53]. In the presence of Fe_2O_3, it might be correlated to the interaction of nitrile (N1s at ca. 399.6 eV) with metal ions (Fe^{3+}, Mn^{4+}, Zn^{2+}). Still, the quantity of this N1s (III) signal is much higher (4.3–4.5 at%) when compared to the signal of metal ions

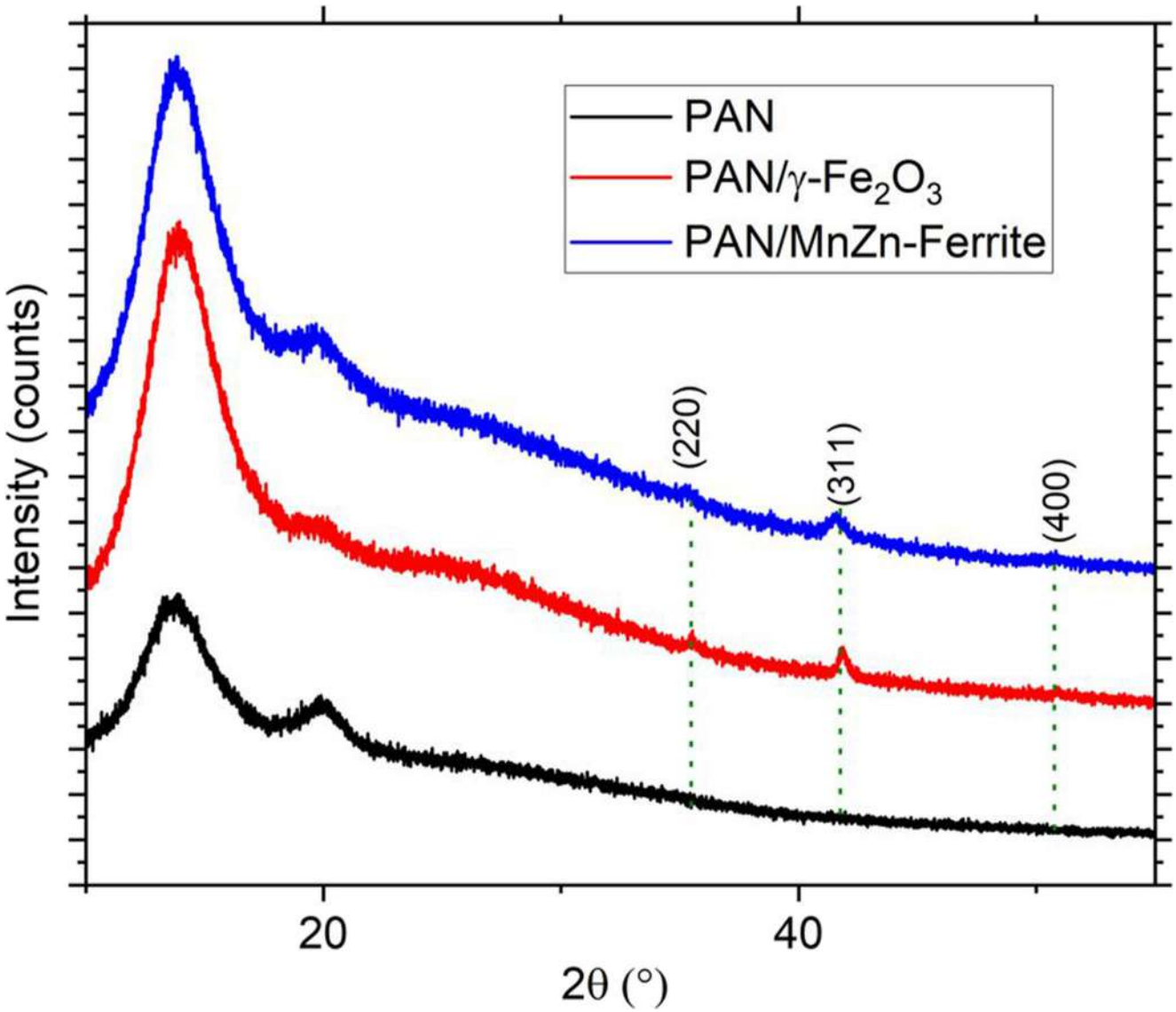

Fig. 4 Structural differences between the considered samples assessed by XRD

(0.7–1 at%, Table S2). Most probably, this signal at ca. 400.7 eV accounts for the new functional groups of nitrogen on the surface. The higher oxidation is also clear from the increase of oxygen to ca. 9.1–11.6 at%. This oxidation after heat treatment is very similar, only slightly higher for PAN (ca. 11.6 at%) than for PAN-containing NPs (9.1–9.6 at%) (Table S2). The presence of NP was confirmed by the signal of Fe2p at ca. 711.3 eV corresponding to Fe^{3+}, Mn2p at ca. 641.8 eV corresponding to Mn^{4+} and Zn2p at ca. 1022.4 eV corresponding to Zn^{2+} (Figure S2).

3.6 Electrochemical behaviour

Two different electrolytic mediums indicate that the ionic double-layer behavior differs from each other, as shown by EIS measurements. The studies were implemented in a PBS Buffer (pH = 7.4) and 0.5 M H_2SO_4. In Fig. 6, the absolute impedance values of $|Z|$ vs. PAN/γ-Fe_2O_3 and PAN/MnZn-Ferrite containing PAN NFs indicate that two electrolytes display the lowest impedance for the PAN/γ-Fe_2O_3 case at the lowest frequencies. The absolute Z values are derived from the Bode Magnitude plots at the 10 mHz frequency, which represents the quasi-DC resistance due to the low frequency, resembling direct current conditions. For the PAN/γ-Fe_2O_3 in H_2SO_4 and PAN/MnZn-Ferrite in PBS samples, relatively low impedance values are observed at 10 mHz. These values can be contrasted with the higher resistance observed in the MnZn-Ferrite in both electrolytes, but with an exception after ~ 1 Hz frequency for PAN/MnZn-Ferrite in H_2SO_4, indicating the lowest impedance absolute Z value

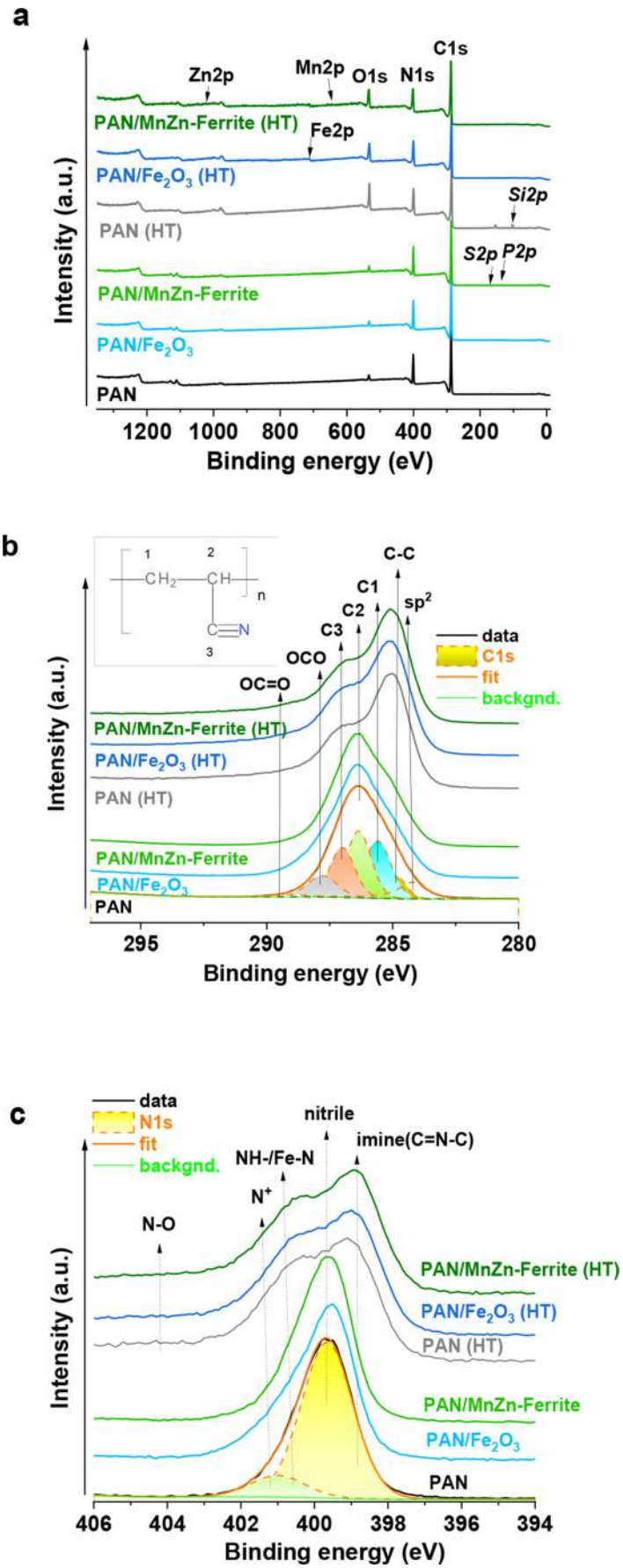

Fig. 5 X-ray photoelectron spectroscopy (**a**) survey spectrum, (**b**) C1s and (**c**) N1s region of PAN, PAN/Fe_2O_3 and PAN/MnZn-Ferrite before and after heat treatment

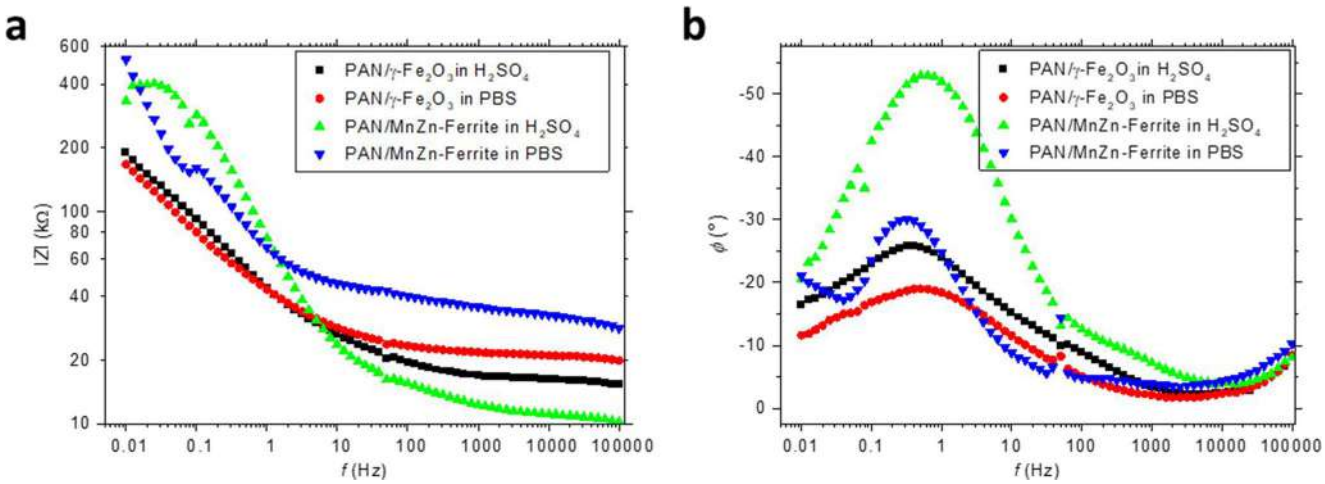

Fig. 6 (**a**) Bode magnitude and (**b**) Bode Phase data in two different electrolytic behaviors within H_2SO_4 and PBS

(resistances) due to the nature of the filler and sulfuric acid. The crossover point for PAN/γ-Fe_2O_3 of the PBS-H_2SO_4 transition is also ~ 1 Hz, but this transition is not as sharp as the PAN/MnZn-Ferrite sample.

The resistances (R_s, R_1, R_2) in the PBS solution tend to be higher compared to those in the H_2SO_4 solution for all samples. PAN/γ-Fe_2O_3 sample shows a higher capacitance compared to PAN/MnZn-Ferrite in 0.5 M solutions of H_2SO_4 and PBS, referring to the higher amount of ion accumulation in bulk form (Table 1). The PAN/MnZn-Ferrite sample in PBS shows a significantly higher R_2 value than in 0.5 M H_2SO_4, indicating a higher impedance. The constant phase element (CPE_1 and CPE_2) values are generally higher in PBS solutions, indicating higher capacitance behavior. The exponents (n_1, n_2) show variability, with lower values in H_2SO_4 solutions, suggesting a more resistive behavior. PAN/MnZn-Ferrite displays lower charge-transfer resistance R_1 in both solutions, referring to higher electron transport from the surface to the bulk layers. On the other hand, the surface has more ion exchange characteristics for the PAN/γ-Fe_2O_3 sample, as confirmed by the surface resistance R_2.

For the bulk-electrolyte interface (R_1, CPE_1 and n_1), a higher capacitance could indicate that more charge is being stored at the interface, which might also mean a higher resistance to charge transfer due to increased interactions at the interface. Nonetheless, the observed inverse relationship between capacitance and resistance in the polarization circuit part (R_2, CPE_2, and n_2) is consistent with electrochemical principles. Higher capacitance suggests improved charge storage and transfer capabilities, which inherently reduce the resistance in the system.

Table 1 Equivalent circuit model of the impedances shown in fig. 6. R_s: solution resistance, CPE_1 and CPE_2: constant phase element exponent associated with bulk layer and polarization, respectively. R_1: charge-transfer resistance, R_2: polarization resistance, n_1 & n_2: constant phase element exponent related to bulk layer and polarization, respectively. χ2: chi-squared error. Sample area = 1 cm^2

R(Q(R(QR)))	PAN/Fe_2O_3 in 0.5 M H_2SO_4	PAN/MnZn-Ferrite in 0.5 M H_2SO_4	PAN/Fe_2O_3 in 0.5 M PBS	PAN/MnZn-Ferrite in 0.5 M PBS
R_s/Ω	$1.59*10^4$	$1.05*10^4$	$2.13*10^4$	$3.16*10^4$
CPE_1/Ss^n	$6.31*10^{-6}$	$2.40*10^{-6}$	$1.01*10^{-5}$	$3.41*10^{-6}$
n_1	0.53	0.57	0.55	0.44
R_1/Ω	$2.38*10^4$	$1.07*10^4$	$6.99*10^4$	$1.74*10^4$
CPE_2/Ss^n	$7.03*10^{-6}$	$1.56*10^{-6}$	$1.82*10^{-5}$	$4.45*10^{-6}$
n_2	0.58	0.85	0.84	0.73
R_2/Ω	$1.88*10^5$	$6.40*10^5$	$7.51*10^4$	$4.68*10^5$
Chi-squared / χ2	$1.02*10^{-3}$	$4.65*10^{-3}$	$4.31*10^{-3}$	$1.20*10^{-2}$

3.7 Magnetic behaviour

Room-temperature magnetic hysteresis loops of the PAN/Fe_2O_3 (black squares) and PAN/MnZn-Ferrite (red dots) samples are depicted in Fig. 7. The M(H) curves have been adjusted based on the mass of the nanocomposite, which includes the electrospun NFs and the magnetic nanoparticles contained therein. Both M(H) curves exhibit a well-defined sigmoidal shape, indicating a smooth magnetization reversal dominated by a rotational process that ends in full magnetic saturation at 10 kOe. The saturation magnetization (M_s) values are 6.4 and 2.3 emu/g for the PAN/Fe_2O_3 and PAN/MnZn-Ferrite samples, respectively. Therefore, the PAN/Fe_2O_3 sample, which includes only Fe ions in the oxide structure, shows a higher magnetic signal strength compared to PAN/MnZn-Ferrite, which also contains non-magnetic Zn ions. The inset of Fig. 7 magnifies the low-field region of the M(H) curves, revealing the hysteretic behavior of both samples. Specifically, the magnetization remanence (M_r) values are 1.1 and 0.1 emu/g, while the coercive field (H_c) values are 106 and 23 Oe for the PAN/Fe_2O_3 and PAN/MnZn-Ferrite samples, respectively. Thus, the MnZn-Ferrite nanoparticles exhibit a reduced effective magnetic anisotropy.

3.8 Cytocompatibility

Since Fe_2O_3/PAN NF and MnZn-Ferrite NPs/PAN NF are intended for biomedical applications, as discussed earlier, it is crucial to ensure their cytocompatibility. The nanoparticles incorporated into PAN may influence cellular responses either positively or negatively, depending on their concentration and interaction with cells. To assess this, cytocompatibility analyses were conducted using the direct method with MSCs.

Figure 8 illustrates the cytocompatibility of MSCs cultivated directly on the samples. A comparison of the cellular metabolic functions of cultivated cells on the materials revealed a significant difference between PAN/MnZn-Ferrite and both PAN and PAN/Fe_2O_3 during the first 24h ($p<0.05$).

This significant reduction in cells' metabolic activity on PAN/MnZn-Ferrite may be attributed to the release of manganese and/or zinc ions and their subsequent uptake by cells. While the exact contribution to cell cytotoxicity

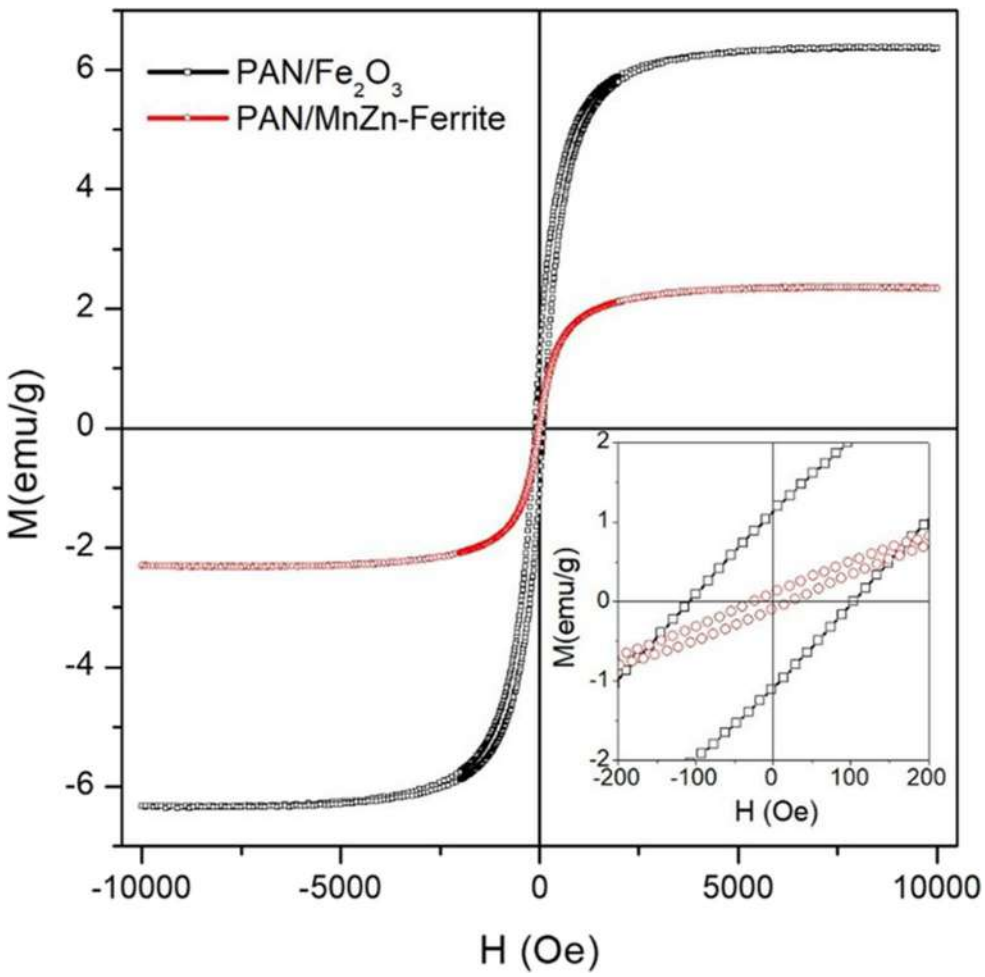

Fig. 7 Room-temperature magnetic hysteresis loops of the PAN/Fe_2O_3 (black squares) and PAN/MnZn-Ferrite (red dots) samples; inset: low magnetic field enlargement

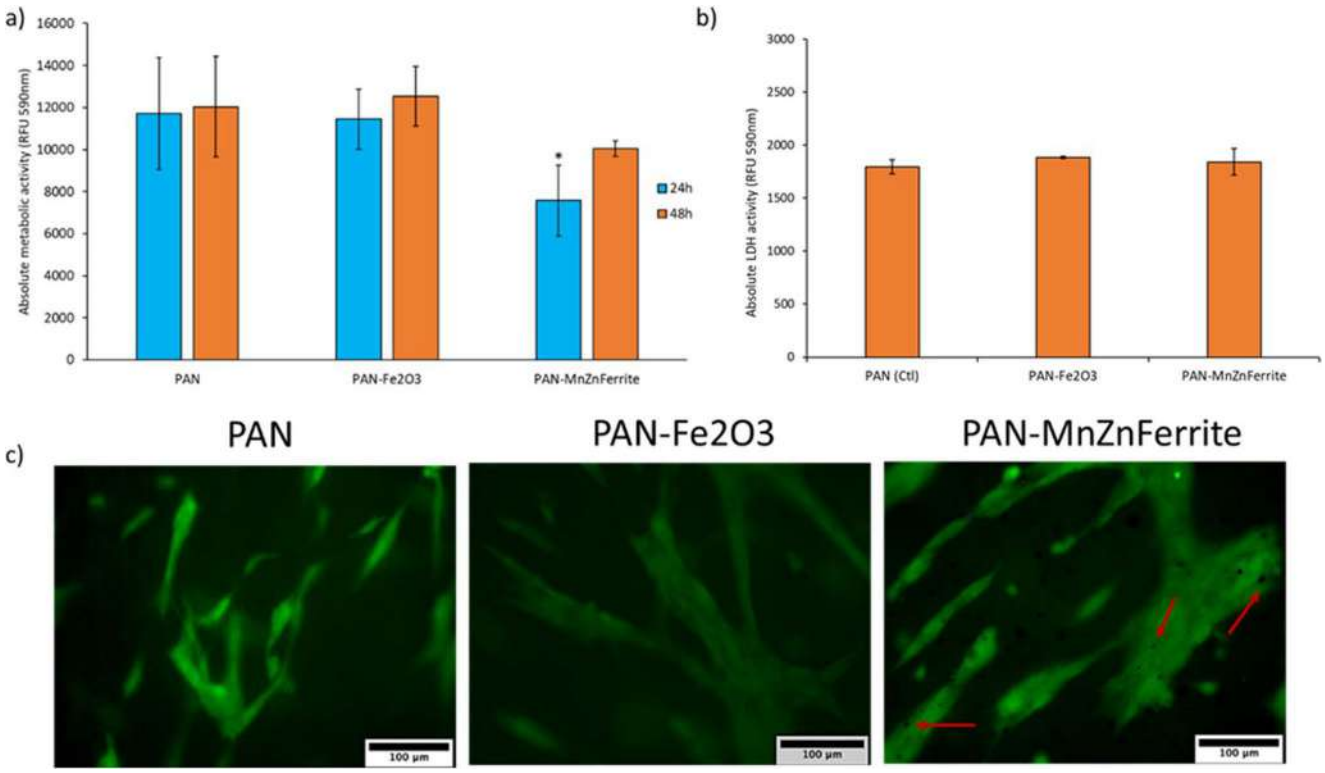

Fig. 8 Direct cytocompatibility evaluation of PAN NF, PAN/Fe_2O_3, and PAN/MnZn-Ferrite samples. hMSCs were cultured directly on the sample surfaces for 24 and 48 h, and cytocompatibility was assessed through the following: (**a**) absolute metabolic activity of hBMSCs, (**b**) Absolute LDH activity measured after 48 h in hMSCs cultured on unloaded (PAN, control) and loaded materials (PAN/Fe_2O_3 and PAN/MnZn-Ferrite); (**c**) Live/Dead imaging after 48 h of cultivation. *$p < 0.05$ PAN vs. and PAN/Fe_2O_3 and PAN/MnZn-Ferrite. Red arrows: MnZn-ferrite NPs

remains unclear, some research suggests that these ions could induce mitochondrial dysfunction, potentially impairing cellular metabolism [66–68].

However, at the second time point (48 h), the significant difference observed earlier disappeared, thus indicating the material's cytocompatibility. These results were further confirmed by the LDH assay, which did not show any significant difference and, consequently, any difference in terms of LDH release between cells cultivated on the control material and the doped samples. The viability of cells is lastly ensured by the Live/Dead assay conducted at the final time point, which showed that all observed cells were alive and displayed a morphology comparable to that of cells grown on the other materials, i.e. hBMSCs cultured on nanostructured TiO_2 [69], Ti-based coatings/Si [70], electrospun PCL/collagen/HA scaffolds [71], polydopamine-coated PDMS [72], and hydroxyapatite/chitosan scaffolds [73]. The Limited increase in viability observed between 24 and 48 h on pure PAN nanofibers reflects the material's limited bioactivity and lack of biochemical cues for hBMSC proliferation. This behavior is in contrast to the MnZn-Ferrite and Fe_2O_3-loaded PAN samples, which showed enhanced biological response supported by multiple assays. The red arrows in Fig. 8c designate black spots corresponding to aggregated MnZn-Ferrite particles which inherently appear as dark-colored under fluorescence microscopy.

The comparison of all samples under identical conditions (same cell suspension, same adhesion period, same medium volume and incubation conditions) using hMSCs directly seeded on the nanofiber membranes. The Alamar Blue values for PAN were sufficiently high, and PAN is well known for its cytocompatibility, which provided sufficient confidence to proceed with the experiments. Moreover, prior studies using hBMSCs on tissue culture polystyrene (TCPS) and calibrated Alamar Blue assays report substantially larger early (24→48 h) increases in metabolic activity than we observed on PAN, ascertained by the reduced hMSC proliferation on non-bioactive material (Jha et al., Fig. 6 in [74]; Begum et al., Fig. S3 in [75]). Taken together with Live/Dead and morphology data showing viable, poorly proliferative cells on PAN, these lines of evidence support the interpretation that the limited increase in viability on pure PAN reflects limited bioactivity and the lack of biochemical proliferative cues. Fig. S3 depicts the Live/Dead fluorescence image of the cells proliferated on the TCPS substrate (control), resembling the cell proliferation on PAN. In terms

of LDH release (Fig. S4) and EdU incorporation (Fig. S5), the monolayer control study was conducted with the polystyrene bottom of the multiwell, where the PAN substrate and control study were shown to be substantially identical.

In summary, the Alamar Blue assay showed only modest changes for PAN between 24 h and 48 h, the LDH assay at 48 h confirmed the absence of cytotoxicity. Furthermore, the Live/Dead imaging showed viable cells with normal morphology.

SEM images in Fig. 9a confirm proper cell adhesion, morphology, and spreading on the nanofibers. Notably, a higher cell density is observed on both doped materials compared to the control. The zoomed-in images further highlight distinct points of contact between the cells and the doped materials, demonstrating the scaffolds' ability to create a favorable environment for cell attachment and growth. Figure 9b and c show that the expression levels of Cadherin-1 and Ki67—key markers of cell adhesion and proliferation, respectively—are significantly higher in cells cultured on PAN/MnZn-Ferrite and PAN/Fe_2O_3 than in those cultured on undoped PAN (**$p<0.01$ and *$p<0.05$, respectively). Previous studies suggest that both iron oxide nanoparticles and MnZn ferrite composites can enhance cell adhesion and proliferation on electrospun substrates by increasing the surface roughness of the NFs, promoting protein adsorption, and improving the hydrophilicity of the resulting scaffold [76, 77]. Figure 9d reports the results related to the Click it EdU proliferation assay. Results demonstrated that cell

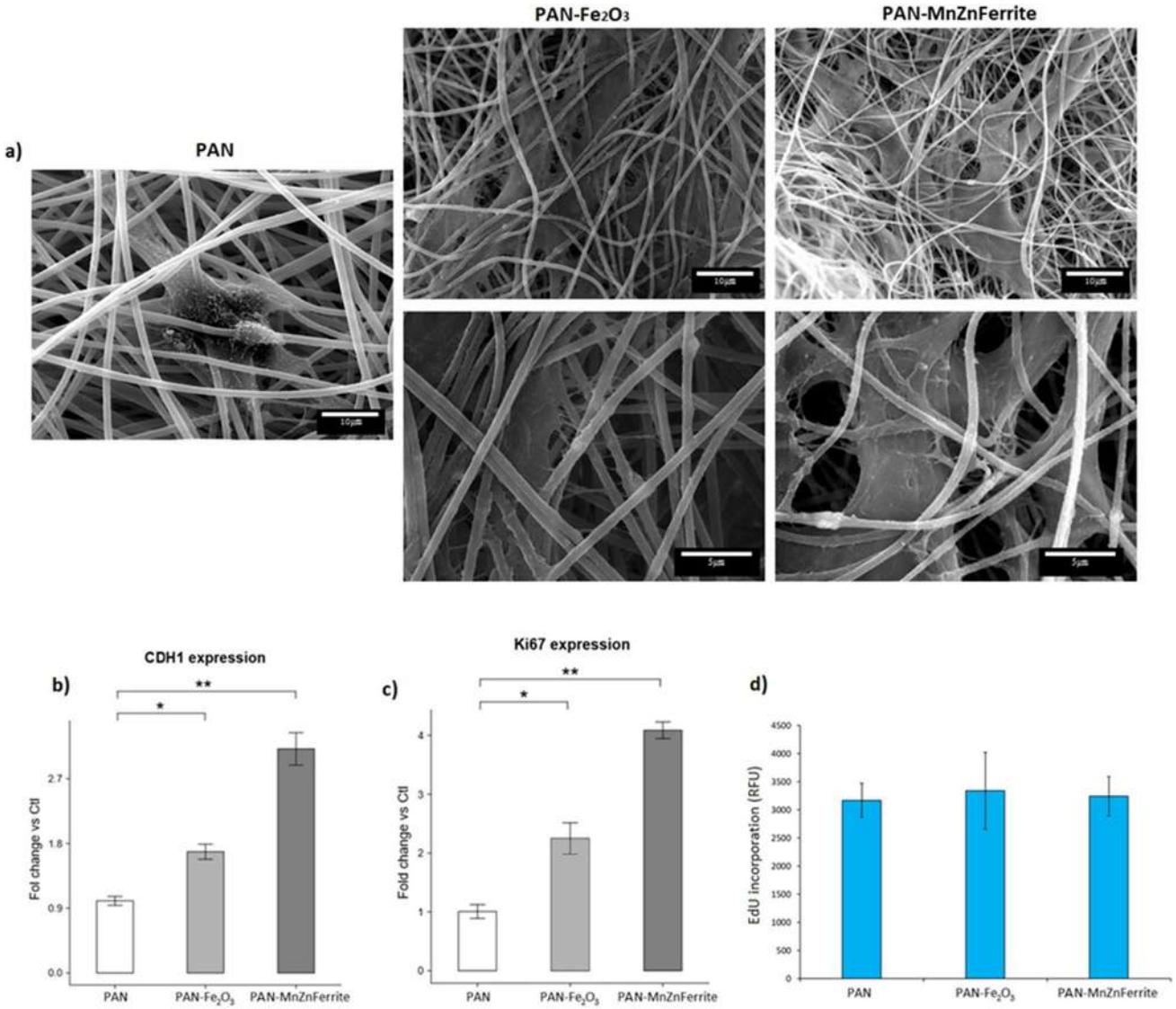

Fig. 9 Cell adhesion and proliferation. (**a**) Representative images showing hMSC attachment on the sample surfaces after 48 h of incubation. (**b-c**) Relative expression of Cadherin-1 (CDH1) and Ki67 in hMSCs cultured on PAN/Fe_2O_3 and PAN/MnZn Ferrite compared to PAN (control); (**d**) EdU-based proliferation assay. *$p<0.05$ **$p<0.01$

proliferation is preserved in all the materials and that there are no significant differences among the groups. The discrepancy between Click-iT and Ki67 results (panel c) may reflect differences in cell cycle distribution. Indeed, the Click-iT detects only cells in the S phase of the cell cycle, while Ki67 indicates overall proliferative activity, including G1, G2, and M phases [78, 79].

Inclusion of $MnZnFe_2O_4$ nanoparticles in PAN NFs enhances hMSC adhesion and spreading compared with Fe_2O_3 at the same loading. The different ionic radii of Mn^{2+}, Zn^{2+}, and Fe^{3+} mean the surface can present a more diverse array of potential interaction sites and variable surface charge for protein ligands [80, 81]. Furthermore, the controlled release of Mn^{2+} and Zn^{2+} ions—both known to support osteogenic differentiation—further stimulates hMSC proliferation and lineage commitment, effects not achievable with the simpler Fe^{3+}-dominated surface of Fe_2O_3 [82, 83].

4 Conclusions

This study's key outcomes can be outlined as follows:

- Uniform electrospun PAN NFs with well-dispersed Fe_2O_3 and MnZn-Ferrite nanoparticles were produced, which possess controlled fiber diameter and homogeneous nanoparticle distribution.
- Advanced characterization techniques, XPS confirmed the structure of PAN NFs and revealed increased oxidation and graphitic carbon content after heat treatment. Using XPS and FTIR, new nitrogen functionalities and interactions between the polar nitrile groups of PAN and Fe_2O_3 and MnZn-Ferrite nanoparticles were confirmed. PAN/MnZn-Ferrite NFs demonstrates smaller magnetic remanence and coercivity compared to PAN/Fe_2O_3 referring to reduced magnetic anisotropy.
- Absolute metabolic and LDH activity tests demonstrated that MnZn-Ferrite and Fe_2O_3 nanoparticles loaded onto PAN NFs remarkably enhanced the viability or conformation of human mesenchymal stromal cells in comparison to the reference PAN sample, making them a promising materials for biomedical applications.
- As compared to PAN and PAN/Fe_2O_3 NFs, Cadherin-1 and Ki67—core identifiers of cell adhesion and proliferation, respectively—are remarkably higher in cells cultured on PAN/MnZn-Ferrite, as also evidenced by SEM images revealing hMSC attachment on the sample surfaces after 48 h of incubation.

These positive, albeit preliminary, biological findings, combined with the intrinsic magnetic properties of the incorporated nanoparticles, suggest the potential for this material to be exploited in the field of magnetic resonance imaging, targeted drug administration, and magnetic hyperthermia for oncology, as well as other advanced therapeutic and diagnostic applications.

Supplementary Information The online version contains supplementary material available at https://doi.org/10.1007/s42247-025-01247-w.

Acknowledgments This work is dedicated to the memory of Prof. Dr. Maria Omastova, whose invaluable contributions were essential to the success of this collaboration. A distinguished scholar in polymers, polymeric composites, and XPS characterization, Prof. Dr. Omastova passed away on May 9, 2024, before this paper's publication. Her expertise and dedication to international scientific collaboration will be deeply missed.

Funding Open access funding provided by Montanuniversität Leoben. This research was partially funded by the Slovak agency VEGA grant number 02/006/22. The authors would like to acknowledge the contribution of the COST Action CA21155 (HISTRATE).

Data availability All data is presented in the figures, graphics and tables in the context of the manuscript.

Declarations

Competing interests The authors declare that they have no known competing financial interests or personal relationships that could have appeared to influence the work reported in this paper.

References

1. A. Heymer, D. Haddad, M. Weber, U. Gbureck, P.M. Jakob, J. Eulert, U. Nöth, Iron oxide labelling of human mesenchymal stem cells in collagen hydrogels for articular cartilage repair. Biomaterials. **29**, 1473–1483 (2008). https://doi.org/10.1016/j.biomaterials.2007.12.003
2. N. Wang, Y. Xie, Z. Xi, Z. Mi, R. Deng, X. Liu, R. Kang, X. Liu, Hope for bone regeneration: the versatility of iron oxide nanoparticles. Front. Bioeng. Biotechnol. (2022). https://doi.org/10.3389/fbioe.2022.937803
3. L.M. Gradinaru, S. Vlad, R.C. Ciobanu, The development and study of some composite membranes based on polyurethanes and iron oxide nanoparticles. Membranes. **12**, 1127 (2022). https://doi.org/10.3390/membranes12111127
4. H. Sadeghzadeh, H. Dianat-Moghadam, A.R. Del Bakhshayesh, D. Mohammadnejad, A. Mehdipour, A review on the effect of

nanocomposite scaffolds reinforced with magnetic nanoparticles in osteogenesis and healing of bone injuries. Stem Cell Res. Ther. **14**, 194 (2023). https://doi.org/10.1186/s13287-023-03426-0
5. K. Kizilbey, E.N. Koprulu, H. Temur, S. Canim Ates, S. Ozer, Magnetic and biomedical properties of iron nanoparticles synthesized using *vitex agnus-castus* extract. Materials **17**, 6064 (2024). https://doi.org/10.3390/ma17246064
6. P. Hu, J. Lu, C. Li, Z. He, X. Wang, Y. Pan, L. Zhao, Injectable magnetic hydrogel filler for synergistic bone tumor hyperthermia chemotherapy. ACS Appl. Bio Mater. **7**, 1569–1578 (2024). https://doi.org/10.1021/acsabm.3c01074
7. J. Nowak-Jary, A. Plociennik, B. Machnicka, Functionalized magnetic Fe_3O_4 nanoparticles for targeted methotrexate delivery in ovarian cancer therapy. Int. J. Mol. Sci. **25**, 9098 (2024). https://doi.org/10.3390/ijms25169098
8. M. Kasprzyk, G. Opila, A. Hinz, S. Stankiewicz, M. Bzowska, K. Wolski, J. Dulinska-Litewka, J. Przewoznik, C. Kapusta, A. Karewicz, Hyaluronic acid-Coated spions with attached folic acid as potential T2 MRI contrasts for anticancer therapies. ACS Appl. Mater. Interfaces. **17**, 9059–9073 (2025). https://doi.org/10.1021/acsami.4c20101
9. L. Maldonado-Camargo, M. Unni, C. Rinaldi, Magnetic characterization of iron oxide nanoparticles for biomedical applications. Methods Mol. Biol. **1570**, 47–71 (2017). https://doi.org/10.1007/978-1-4939-6840-4_4
10. Q. Wang, B. Chen, F. Ma, S. Lin, M. Cao, Y. Li, N. Gu, Magnetic iron oxide nanoparticles accelerate osteogenic differentiation of mesenchymal stem cells via modulation of long noncoding RNA INZEB2. Nano Res. **10**, 626–642 (2017). https://doi.org/10.1007/s12274-016-1322-4
11. J. Nowak-Jary, In vivo biodistribution and clearance of magnetic iron oxide nanoparticles for medical applications. Int. J. Nanomed. **18**, 4067–4100 (2023). https://doi.org/10.2147/IJN.S415063
12. S. Kargozar, F. Baino, S. Hamzehlou, M.R. Hamblin, M. Mozafari, Nanotechnology for angiogenesis: opportunities and challenges. Chem. Soc. Rev. **49**, 5008–5057 (2020). https://doi.org/10.1039/c8cs01021h
13. A. Shradhanjali, J.T. Wolfe, B.J. Tefft, Magnetic cell targeting for cardiovascular tissue engineering, tissue eng. Part. B Rev. (2024). https://doi.org/10.1089/ten.TEB.2024.0103
14. H.O. Alsaab, A.S. Al-Hibs, R. Alzhrani, K.K. Alrabighi, A. Alqathama, A. Alwithenani, A.H. Almalki, Y.S. Althobaiti, Nanomaterials for antiangiogenic therapies for cancer: a promising tool for personalized medicine. Int. J. Mol. Sci. **22**, 1631 (2021). https://doi.org/10.3390/ijms22041631
15. O. Agboola, O.S.I. Fayomi, A. Ayodeji, A.O. Ayeni, E.E. Alagbe, S.E. Sanni, E.E. Okoro, L. Moropeng, R. Sadiku, K.W. Kupolati, B.A. Oni, A review on polymer nanocomposites and their effective applications in membranes and adsorbents for water treatment and gas separation. Membranes. **11**, 139 (2021). https://doi.org/10.3390/membranes11020139
16. A. Luzio, E.V. Canesi, C. Bertarelli, M. Caironi, Electrospun polymer fibers for electronic applications. Materials **7**, 906–947 (2014). https://doi.org/10.3390/ma7020906
17. S. Ma, A. Li, L. Pan, Application progress of multi-functional polymer composite nanofibers based on electrospinning: a brief review. Polymers **16**, 2459 (2024). https://doi.org/10.3390/polym16172459
18. S.M.S. Shahriar, J. Mondal, M.N. Hasan, V. Revuri, D.Y. Lee, Y.-K. Lee, Electrospinning Nanofibers Ther. Delivery Nanomaterials. **9**, 532 (2019). https://doi.org/10.3390/nano9040532
19. T. Maeda, Y.-J. Kim, T. Aoyagi, M. Ebara, The design of temperature-responsive nanofiber meshes for cell storage applications. Fibers **5**, 13 (2017). https://doi.org/10.3390/fib5010013
20. D.T. Govindaraju, H.H. Kao, Y.M. Chien, J.P. Chen, Composite polycaprolactone/gelatin nanofiber membrane scaffolds for mesothelial cell culture and delivery in mesothelium repair. Int. J. Mol. Sci. **25**, 9803 (2024). https://doi.org/10.3390/ijms25189803
21. S. Pisani, A. Piazza, R. Dorati, I. Genta, M. Rosalia, E. Chiesa, G. Bruni, R. Migliavacca, B. Conti, Investigating electrospun shape memory patches as gentamicin drug delivery system. Int. J. Pharm. , 125393 (2025). https://doi.org/10.1016/j.ijpharm.2025.125393
22. Z. Moazzami Goudarzi, A. Zaszczyńska, T. Kowalczyk, P. Sajkiewicz, Electrospun antimicrobial drug delivery systems and hydrogels used for wound dressings. Pharmaceutics. **16**, 93 (2024). https://doi.org/10.3390/pharmaceutics16010093
23. D. Coetzee, M. Venkataraman, J. Militky, M. Petru, Influence of nanoparticles on thermal and electrical conductivity of composites. Polymers. **12**, 742 (2020). https://doi.org/10.3390/polym12040742
24. Y.R.V. Shih, C.N. Chen, S.W. Tsai, Y.J. Wang, O.K. Lee, Growth of mesenchymal stem cells on electrospun type I collagen nanofibers. Stem Cells. **24**, 2391–2397 (2006). https://doi.org/10.1634/stemcells.2006-0253
25. R.A. Neal, S.G. McClugage, M.C. Link, L.S. Sefcik, R.C. Ogle, E.A. Botchwey, Laminin nanofiber meshes that mimic morphological properties and bioactivity of basement membranes. Tissue Eng. Part. C **15**, 11–21 (2009). https://doi.org/10.1089/ten.tec.2007.0366
26. J.M. Coburn, M. Gibson, S. Monagle, Z. Patterson, J.H. Elisseeff, Bioinspired nanofibers support chondrogenesis for articular cartilage repair. Proc. Natl. Acad. Sci. U. S. A. **109**, 10012–10017 (2012). https://doi.org/10.1073/pnas.1121605109
27. Y.M. Kolambkar, A. Peister, A.K. Ekaputra, D.W. Hutmacher, R.E. Guldberg, Colonization and osteogenic differentiation of different stem cell sources on electrospun nanofiber meshes. Tissue Eng. Part A **16**, 3219–3230 (2010). https://doi.org/10.1089/ten.TEA.2010.0004
28. H.-H. Kao, D.T. Govindaraju, B.S. Dash, J.-P. Chen, Electrospun aligned gelatin/chitosan nanofibrous membranes for a better culture of mesothelial cells. J. Compos. Sci. **9**, 31 (2025). https://doi.org/10.3390/jcs9010031
29. D. Jhala, H.A. Rather, R. Vasita, Extracellular matrix mimicking polycaprolactone-chitosan nanofibers promote stemness maintenance of mesenchymal stem cells via spheroid formation. Biomed. Mater. **15**, 035011 (2020). https://doi.org/10.1088/1748-605X/ab772e
30. D. Yu, J. Wang, K.- Qian, J. Yu, H.- Zhu, Effects of nanofibers on mesenchymal stem cells: environmental factors affecting cell adhesion and osteogenic differentiation and their mechanisms. J. Zhejiang Univ. Sci. B. **21**, 871–884 (2020). https://doi.org/10.1631/jzus.B2000355
31. T.A. Adegbola, O. Agboola, O.S.I. Fayomi, Review of polyacrylonitrile blends and application in manufacturing technology: recycling and environmental impact. Results Eng **7**, 100144 (2020). https://doi.org/10.1016/j.rineng.2020.100144
32. X. Chen, Y. Su, F. Shen, Y. Wan, Antifouling ultrafiltration membranes made from PAN-b-PEG copolymers: effect of copolymer composition and PEG chain length. J. Membr. Sci. **384**, 44–51 (2011). https://doi.org/10.1016/j.memsci.2011.09.002
33. T. Blachowicz, A. Ehrmann, Conductive electrospun nanofiber Mats. Materials. **13**, 152 (2020). https://doi.org/10.3390/ma13010152
34. M.Q. Khan, M.A. Alvi, H.H. Nawaz, M. Umar, Cancer Treat. Using Nanofibers: Rev. Nanomaterials. **14**, 1305 (2024). https://doi.org/10.3390/nano14151305
35. X. Li, L. Wang, S. Li, S. Yu, Z. Liu, Q. Liu, X. Dong, In situ growth of HKUST-1 on electrospun polyacrylonitrile nanofibers/regenerated cellulose aerogel for efficient methylene blue adsorption. Int. J. Biol. Macromol. **274**, 133381 (2024). https://doi.org/10.1016/j.ijbiomac.2024.133381

36. C. Huang, X. Xu, J. Fu, D.-G. Yu, Y. Liu, Recent progress in electrospun polyacrylonitrile nanofiber-based wound dressing. Polymers **14**, 3266 (2022). https://doi.org/10.3390/polym14163266
37. N. Sirelkhatim, A. Parveen, D. LaJeunesse, D. Yu, L. Zhang, Polyacrylonitrile nanofibrous mat from electrospinning: born with potential anti-fungal functionality. Eur. Polym. J. **119**, 176–180 (2019). https://doi.org/10.1016/j.eurpolymj.2019.07.035
38. Y. Mei, C. Yao, K. Fan, X. Li, Surface modification of polyacrylonitrile nanofibrous membranes with superior antibacterial and easy-cleaning properties through hydrophilic flexible spacers. J. Membr. Sci. (2012). https://doi.org/10.1016/j.memsci.2012.06.021
39. S. Homaeigohar, T.-Y. Tsai, E.S. Zarie, M. Elbahri, T.-H. Young, A.R. Boccaccini, Bovine serum albumin (BSA)/polyacrylonitrile (PAN) biohybrid nanofibers coated with a biomineralized calcium deficient hydroxyapatite (HA) shell for wound dressing. Mater. Sci. Eng. C **116**, 111248 (2020). https://doi.org/10.1016/j.msec.2020.111248
40. C. Barozzi, G. Cairo, R. Fumero, S. Scuri, M.C. Tanzi, P. Albonico, Polyacrylonitrile membranes in hemodialysis: blood-surface interactions. Life Support Syst **3 Suppl 1**, 490–494 (1985). https://doi.org/10.1016/0376-7388(88)80019-X
41. A. Mamun, L. Sabantina, Electrospun magnetic nanofiber mats for magnetic hyperthermia in cancer treatment applications—technology, mechanism, and materials. Polymers **15**, 1902 (2023). https://doi.org/10.3390/polym15081902
42. M.R. Ramezani, Z. Ansari-Asl, E. Hoveizi, A.R. Kiasat, Polyacrylonitrile/Fe(III) metal-organic framework fibrous nanocomposites designed for tissue engineering applications. Mater. Chem. Phys. **229**, 242–250 (2019). https://doi.org/10.1016/j.matchemphys.2019.03.031
43. L.M. Bauer, S.F. Situ, M.A. Griswold, A.C.S. Samia, High-performance iron oxide nanoparticles for magnetic particle imaging – guided hyperthermia (hMPI). Nanoscale. **8**, 12162–12169 (2016). https://doi.org/10.1039/C6NR01877G
44. C. Pucci, A. Degl'Innocenti, M. Belenli, G. Gümüş, Ciofani, Superparamagnetic iron oxide nanoparticles for magnetic hyperthermia: recent advancements, molecular effects, and future directions in the omics era. Biomaterials Sci. **10**, 2103–2121 (2022). https://doi.org/10.1039/D1BM01963E
45. N. Zhu, H. Ji, C. Shen, J. Wu, J. Niu, J. Yang, M.U. Farooq, H. Li, X. Niu, Study of alternating magnetic heating characteristics of MnZn ferrite nanoparticles for magnetic hyperthermia applications. IEEE Trans. Appl. Supercond. **29**, 1–5 (2019). https://doi.org/10.1109/TASC.2018.2882416
46. A.K. Graciano Alvarez, M. Dotter, K. Tuvshinbayar, L. Bondzio, I. Ennen, A. Hütten, T. Blachowicz, A. Ehrmann, Electrospinning poly(acrylonitrile) containing magnetite nanoparticles: influence of magnetite contents. Fibers **12**, 19 (2024). https://doi.org/10.3390/fib12030019
47. V. Herynek, K. Turnovcová, A. Gálisová, O. Kaman, D. Mareková, J. Koktan, M. Vosmanská, L. Kosinová, P. Jendelová, Manganese-zinc ferrites: safe and efficient nanolabels for cell imaging and tracking in vivo. Chemistryopen **8**, 155–165 (2019). https://doi.org/10.1002/open.201800261
48. J. Leng, J. Li, J. Ren, L. Deng, C. Lin, Star–block copolymer micellar nanocomposites with Mn,Zn-doped nano-ferrite as superparamagnetic MRI contrast agent for tumor imaging. Mater. Lett. **152**, 185–188 (2015). https://doi.org/10.1016/j.matlet.2015.03.120
49. T. Sobhani, D. Shahbazi-Gahrouei, M. Rostami, M. Zahraei, A. Farzadniya, Assessment of Manganese-Zinc ferrite nanoparticles as a novel magnetic resonance imaging contrast agent for the detection of 4T1 breast cancer cells. J. Med. Signals Sens. **9**, 245–251 (2019). https://doi.org/10.4103/jmss.JMSS_59_18
50. E.M. Materón, C.M. Miyazaki, O. Carr, N. Joshi, P.H.S. Picciani, C.J. Dalmaschio, F. Davis, F.M. Shimizu, Magnetic nanoparticles in biomedical applications: a review. Appl. Surf. Sci. Adv. **6**, 100163 (2021). https://doi.org/10.1016/j.apsadv.2021.100163
51. K. Huner, B. Sarac, E. Yüce, A. Rezvan, M. Micusik, M. Omastova, J. Eckert, A.S. Sarac, Iron oxide – poly(m-anthranilic acid)–poly(ε-caprolactone) electrospun composite nanofibers: fabrication and properties. Mol. Syst. Des. Eng. **8**, 394–406 (2023). https://doi.org/10.1039/D2ME00181K
52. S. Gumrukcu, V. Soprunyuk, B. Sarac, E. Yüce, J. Eckert, A.S. Sarac, Electrospun polyacrylonitrile/2-(acryloyloxy)ethyl ferrocenecarboxylate polymer blend nanofibers. Mol. Syst. Des. Eng. **6**, 476–492 (2021). https://doi.org/10.1039/d1me00008j
53. B. Sarac, V. Soprunyuk, G. Herwig, S. Gümrükçü, E. Kaplan, E. Yüce, W. Schranz, J. Eckert, L.F. Boesel, A.S. Sarac, Thermomechanical properties of confined magnetic nanoparticles in electrospun polyacrylonitrile nanofiber matrix exposed to a magnetic environment: structure, morphology, and stabilization. Nanoscale Adv. **6**, 6184–6195 (2024). https://doi.org/10.1039/d4na00631c
54. Q. Liu, N. Xu, L. Fan, A. Ding, Q. Dong, Polyacrylonitrile (PAN)/TiO_2 mixed matrix membrane synthesis by thermally induced self-crosslinking for thermal and organic-solvent resistant filtration. Chem. Eng. Sci. **228**, 115993 (2020). https://doi.org/10.1016/j.ces.2020.115993
55. W. Li, Z. Yang, G. Zhang, Q. Meng, Heat-treated polyacrylonitrile (PAN) hollow fiber structured packings in isopropanol (IPA)/water distillation with improved thermal and chemical stability. Ind. Eng. Chem. Res. **52**, 6492–6501 (2013). https://doi.org/10.1021/ie303122u
56. J. Gao, X. Wang, J. Zhang, R. Guo, Preparation of heat-treated PAN/SiO_2 hybrid hollow fiber membrane contactor for acetylene absorption. Sep. Purif. Technol. **159**, 116–123 (2016). https://doi.org/10.1016/j.seppur.2016.01.005
57. G. Zhang, H. Yan, S. Ji, Z. Liu, Self-assembly of polyelectrolyte multilayer pervaporation membranes by a dynamic layer-by-layer technique on a hydrolyzed polyacrylonitrile ultrafiltration membrane. J. Membr. Sci. **292**, 1–8 (2007). https://doi.org/10.1016/j.memsci.2006.11.023
58. S. Nag, S. Pradhan, D. Das, B. Tudu, R. Bandyopadhyay, R.B. Roy, Fabrication of a molecular imprinted polyacrylonitrile engraved graphite electrode for detection of formalin in food extracts. IEEE Sens. J. **22**, 42–49 (2022). https://doi.org/10.1109/JSEN.2021.3128520
59. E. Pullicino, W. Zou, M. Gresil, C. Soutis, The effect of shear mixing speed and time on the mechanical properties of gnp/epoxy composites. Appl. Compos. Mater. **24**, 301–311 (2017). https://doi.org/10.1007/s10443-016-9559-3
60. M. Aliahmad, N. Nasiri Moghaddam, Synthesis of maghemite (γ-Fe_2O_3) nanoparticles by thermal-decomposition of magnetite (Fe_3O_4) nanoparticles. Mater. Sci. -Pol **31**, 264–268 (2013). https://doi.org/10.2478/s13536-012-0100-6
61. S. Agarwal, M.P. Mudoi, S. Singhal, A.S. Khichi, A. Dhyani, 41 - Ferrites and Fe oxides as effective materials for the removal of CO_2, in: J. Pal Singh, K.H. Chae, R.C. Srivastava, O.F. Caltun (Eds.), Ferrite Nanostructured Magnetic Materials, Woodhead Publishing 2023, pp. 831–851
62. Y. Zhao, Z. Zhao, M. Wei, X. Jiang, H. Li, J. Gao, L. Hou, Preparation of Si-doped and cross linked carbon nanofibers via electrospinning and their supercapacitive properties. Prog. Nat. Sci. Mater. Int. **28**, 337–344 (2018). https://doi.org/10.1016/j.pnsc.2018.04.013
63. H.A. Alshamsi, B.S. Hussein, Synthesis, characterization and photocatalysis of g-Fe2O3 nanoparticles for degradation of cibacron brilliant yellow 3G-P. Asian J. Chem. **30**, 273–279 (2017). https://doi.org/10.14233/ajchem.2018.20888

64. D. Arcos, R. Valenzuela, M. Vallet-Regí, M. Vázquez, Grain boundary impedance of doped Mn–Zn ferrites. J. Mater. Res. **14**, 861–865 (1999). https://doi.org/10.1557/JMR.1999.0115
65. G. Beamson, D.R. Briggs, *The XPS of Polymers Database* (Surface Spectra Ltd., 2000)
66. S. Brown, N.L. Taylor, Could mitochondrial dysfunction play a role in manganese toxicity? Environ. Toxicol. Pharmacol. **7**, 49–57 (1999). https://doi.org/10.1016/S1382-6689(98)00054-4
67. J. Diessl, J. Berndtsson, F. Broeskamp, L. Habernig, V. Kohler, C. Vazquez-Calvo, A. Nandy, C. Peselj, S. Drobysheva, L. Pelosi, F.N. Vögtle, F. Pierrel, M. Ott, S. Büttner, Manganese-driven CoQ deficiency. Nat. Commun. **13**, 6061 (2022). https://doi.org/10.1038/s41467-022-33641-x
68. O.R.M. Bagshaw, R. Alva, J. Goldman, J.W. Drelich, J.A. Stuart, 33 - Mitochondrial zinc toxicity, in: M.R. de Oliveira (Ed.), Mitochondrial Intoxication, Academic Press 2023, pp. 723–744
69. M. Vercellino, G. Ceccarelli, F. Cristofaro, M. Balli, F. Bertoglio, G. Bruni, L. Benedetti, M.A. Avanzini, M. Imbriani, L. Visai, Nanostructured TiO_2 surfaces promote human bone marrow mesenchymal stem cells differentiation to osteoblasts. Nanomaterials (2016). https://doi.org/10.3390/nano6070124
70. C. Qu, S. Kaitainen, H. Kröger, R. Lappalainen, M.J. Lammi, Behavior of human bone marrow-derived mesenchymal stem cells on various titanium-based coatings. Materials **9**, 827 (2016). https://doi.org/10.3390/ma9100827
71. M.C. Phipps, W.C. Clem, S.A. Catledge, Y. Xu, K.M. Hennessy, V. Thomas, M.J. Jablonsky, S. Chowdhury, A.V. Stanishevsky, Y.K. Vohra, Bellis, mesenchymal stem cell responses to Bone-Mimetic electrospun matrices composed of polycaprolactone, collagen I and nanoparticulate hydroxyapatite. PLOS ONE. **6**, e16813 (2011). https://doi.org/10.1371/journal.pone.0016813
72. Y.J. Chuah, Y.T. Koh, K. Lim, N.V. Menon, Y. Wu, Y. Kang, Simple surface engineering of polydimethylsiloxane with polydopamine for stabilized mesenchymal stem cell adhesion and multipotency. Sci. Rep. **5**, 18162 (2015). https://doi.org/10.1038/srep18162
73. H. Liu, H. Peng, Y. Wu, C. Zhang, Y. Cai, G. Xu, Q. Li, X. Chen, J. Ji, Y. Zhang, H.W. OuYang, The promotion of bone regeneration by nanofibrous hydroxyapatite/chitosan scaffolds by effects on integrin-BMP/Smad signaling pathway in BMSCs. Biomaterials. **34**, 4404–4417 (2013). https://doi.org/10.1016/j.biomaterials.2013.02.048
74. A.K. Jha, X. Xu, R.L. Duncan, X. Jia, Controlling the adhesion and differentiation of mesenchymal stem cells using hyaluronic acid-based, doubly crosslinked networks. Biomaterials. **32**, 2466–2478 (2011). https://doi.org/10.1016/j.biomaterials.2010.12.024
75. R. Begum, A.W. Perriman, B. Su, F. Scarpa, W. Kafienah, Chondroinduction of mesenchymal stem cells on cellulose-silk composite nanofibrous substrates: the role of substrate elasticity. Front. Bioeng. Biotechnol. **8**, 197 (2020). https://doi.org/10.3389/fbioe.2020.00197
76. C.J. Mortimer, C.J. Wright, The fabrication of iron oxide nanoparticle-nanofiber composites by electrospinning and their applications in tissue engineering. Biotechnol. J. (2017). https://doi.org/10.1002/biot.201600693
77. Y. Wang, Y. Miao, G. Li, M. Su, X. Chen, H. Zhang, Y. Zhang, W. Jiao, Y. He, J. Yi, X. Liu, H. Fan, Engineering ferrite nanoparticles with enhanced magnetic response for advanced biomedical applications. Mater. Today Adv. **8**, 100119 (2020). https://doi.org/10.1016/j.mtadv.2020.100119
78. R.C. Leif, J.H. Stein, R.M. Zucker, A short history of the initial application of anti–5-BrdU to the detection and measurement of S phase. Cytometry A **58A**, 45–52 (2004). https://doi.org/10.1002/cyto.a.20012
79. I. Miller, M. Min, C. Yang, C. Tian, S. Gookin, D. Carter, S.L. Spencer, Ki67 is a graded rather than a binary marker of proliferation versus quiescence. Cell. Rep. **24**, 1105–1112e5 (2018). https://doi.org/10.1016/j.celrep.2018.06.110
80. Y.J. Kim, B.C. Park, Y.S. Choi, M.J. Ko, Y.K. Kim, Quantitative analysis on cellular uptake of clustered ferrite magnetic nanoparticles. Electron. Mater. Lett. **15**, 471–480 (2019). https://doi.org/10.1007/s13391-019-00141-y
81. R. Augustine, A. Hasan, R. Primavera, R.J. Wilson, A.S. Thakor, B.D. Kevadiya, Cellular uptake and retention of nanoparticles: insights on particle properties and interaction with cellular components. Mater. Today Commun. **25**, 101692 (2020). https://doi.org/10.1016/j.mtcomm.2020.101692
82. Y.J. Kim, J. Lee, G.B. Im, J. Song, J. Song, J. Chung, T. Yu, S.H. Bhang, Dual ion releasing nanoparticles for modulating osteogenic cellular microenvironment of human mesenchymal stem cells. Materials. **14**, 412 (2021). https://doi.org/10.3390/ma14020412
83. Z. Du, H. Leng, L. Guo, Y. Huang, T. Zheng, Z. Zhao, X. Liu, X. Zhang, Q. Cai, X. Yang, Calcium silicate scaffolds promoting bone regeneration via the doping of Mg^{2+} or Mn^{2+} ion. composites. Part. B **190**, 107937 (2020). https://doi.org/10.1016/j.compositesb.2020.107937